Int. J. Electrochem. Sci., 17 **(2022)** Article Number: 22124, doi: 10.20964/2022.12.05

International Journal of
ELECTROCHEMICAL
SCIENCE
www.electrochemsci.org

Preparation, phase analysis and electrochemistry of magnetite (Fe_3O_4) and maghemite (γ-Fe_2O_3) nanoparticles

Ebenezer C. Nnadozie, Peter A. Ajibade[*]

School of Chemistry and Physics, University of KwaZulu-Natal, Private Bag X01, Scottsville, Pietermaritzburg, 3209 South Africa.
[*]E-mail: ajibadeP@ukzn.ac.za

Received: 20 June 2022 / *Accepted:* 7 August 2022 / *Published:* 17 November 2022

Magnetite and maghemite superparamagnetic nanoparticles were prepared via co-precipitation synthetic route. The phases of the iron nanoparticles were quantitatively confirmed from their powder X-ray diffraction patterns (XRD) and cyclic voltammetry. UV-Visible, Fourier transform infrared (FT-IR), Energy dispersive X-ray spectroscopy (EDS) and high resolution transmission electron microscopy (HRTEM) were used to differentiate both types of iron nanoparticles. Cyclic voltammetry showed that magnetite nanoparticles exhibited one redox couple while maghemite had both a redox couple and an irreversible anodic peak. The results shows that aqueous ammonia was more desirable for the synthesis of narrow sized and mono-phased magnetite nanoparticles. The iron oxides prepared from sodium hydroxide showed pronounced energy bandgap reduction in comparison to those obtained from aqueous ammonia. Selected area electron diffraction (SAED) patterns of the as-prepared iron oxides nanoparticles confirmed the nanoparticles were crystalline. Superparamagnetism of magnetite nanoparticles was confirmed from the hysteresis loop; magnetisation saturation (Ms) value was 69.3 $emug^{-1}$ while the BET surface area was 110.31 m^2/g. The average particle sizes of the nanoparticles were 13 nm. The bandgap values were 3.9 and 2.6 eV for magnetite and maghemite nanoparticles, respectively.

Keywords: Magnetite; maghemite; phase analysis; cyclic voltammetry; square wave voltammetry

1. INTRODUCTION

Superparamagnetic nanoparticles are nanomaterials with particle sizes in the range 1-40 nm [1, 2]. Typical methods for the synthesis of superparamagnetic nanoparticles include sol-gel reaction, sonochemical, hydrothermal, microwave heating, laser and flame spray pyrolysis, co-precipitation, green or biological route, polyol methods, thermal decomposition, solvothermal, micro-emulsion, combustion synthesis and oxidation method [3-14]. Co-precipitation of iron precursors in stoichiometric amount is an established and vastly scalable route for the preparation of iron oxides nanoparticles [15,

16]. The size distribution of the particles is dependent on pH and ionic strength of the precipitating agent with an alkaline solution being desirable for the formation of spherical and small size iron oxide nanoparticles [17]. Superparamagnetic iron oxide nanoparticles (SPION): Magnetite (Fe_3O_4) and maghemite (γ-Fe_2O_3) have multipurpose usage because of their low toxicity and environmental compatibility [1]. A significant problem in the application of iron oxide nanoparticles is the phase differentiation of maghemite and magnetite nanoparticles [18]. The absolute phase of a nanomaterial is a strategic structural quality that influences its functionality and unique properties [19-21]. Phase pure magnetite or maghemite is required for biomedical applications; the presence of secondary phases will negatively affect the performance of the nanomaterial [22, 23].

Powder X-ray diffraction patterns (XRD) of magnetite and maghemite have been used by several authors to confirm the crystalline phases of the iron oxide nanoparticles [24, 25]. However, considering the similarity of the powder X-ray diffraction patterns for both magnetite and maghemite; it is desirable to examine the powder X-ray diffraction patterns of iron oxides prepared using different techniques. The electrochemical properties of the iron oxide nanoparticles were compared the crystalline phases of the iron oxides nanoparticles. In this work, we report a comparative study on the phase analysis of iron oxide nanoparticles using UV-Visible, FT-IR, EDS, TEM, XRD and cyclic voltammetry. Cyclic voltammetry was adopted as a secondary analytical method for the confirmation of the crystalline phases of the iron oxides nanoparticles.

2. MATERIALS AND METHOD

All chemicals used in the experiments were of analytical grade and used without further purification. Iron(III) chloride hexahydrate ($FeCl_3{\cdot}6H_2O$; CAS:10025-77-1); iron(II) chloride tetrahydrate ($FeCl_2{\cdot}4H_2O$; CAS: 13478); sodium hydroxide (NaOH; CAS:1310-73-2); and aqueous ammonia ($NH_3.H_2O$; CAS: 1336-21-6) were purchased from Sigma-Aldrich South Africa. Deionised water with resistivity value of 10.7 Ω cm^{-1} from the School of Chemistry and Physics, University of Kwazulu-Natal South Africa was used as working solvent. The methods of co-precipitation of metals from dilute solution as reported by Wanjeri *et al.* was adopted [26].

2.1 Synthesis of iron oxides nanoparticles

The alkaline synthetic medium was compared using both sodium hydroxide and aqueous ammonia; the reaction conditions presented in Table 1 were adopted. Magnetite and maghemite were prepared using 1:2 and 1:1 molar ratio of iron(II) and Iron(III) precursors, respectively. Magnetite was synthesised using 1g of $FeCl_2{\cdot}4H_2O$ and 2.7g $FeCl_3{\cdot}6H_2O$, while maghemite was prepared using 1.04 g and 1.08 g each of $FeCl_2{\cdot}4H_2O$ and $FeCl_3{\cdot}6H_2O$ respectively. The granules were solvated using 50 mL of freshly boiled deionised water and quantitatively transferred to a three-neck round bottom flask. The mixture was stirred for 30 min; followed by the addition of 1M freshly prepared NaOH or 28% aqueous ammonia drop-wisely (6 mL/min) till pH 12 was reached. The ageing process was completed after 1 h

under the continuous flow of nitrogen gas. The obtained product was allowed to cool to room temperature and washed severally with deionised water and finally acetone. The as-prepared iron oxide nanoparticle was dried at 70 ± 10 ºC for 6 h in an electric oven.

Table 1. Reaction condition for nanoparticles syntheses

Nos	Precipitating base	Reaction conditions
1.	1M NaOH	500 rpm, 2h, 100°C
2.	28% $NH_3 \cdot H_2O$	500 rpm, 1h, 70°C

2.2 Physical characterization

Powder X-ray diffraction (XRD) patterns of the nanoparticles were analysed using (XPERT-PRO) within the 2θ angular range of 4.01 to 89.9° and scanning step time of 260 s. Voltammetric studies were conducted using an autolab potentiostat equipped with autolab Nova 1.7 software for data handling. DMSO was used as diluent for the nanoparticles. Before each run, metal solutions were deoxygenated by running a stream of nitrogen gas for 15 min. Tetrabutylammonium tetrafluoroborate ($TBABF_4$) was used as a supporting electrolyte. Cyclic voltammetry was conducted within the potential window of -1.5 to +1.5V.

In contrast, square wave voltammetry (SWV) was conducted by setting the step potential at 4 mV, amplitude at 20 mV and frequency at 25 Hz. HRTEM images were captured on JEOL JEM 2100. Scanning electron microscope (SEM-EVOLS15, ZEISS) equipped with software INCA for EDX analysis was used to report the morphology and the atomic composition of the nanoparticles. LakeShore model 735 vibrating sample magnetometer was utilised in determining magnetisation saturation. Brunauer–Emmett–Tellers surface area (S_{BET}) was carried out on Micromeritics Tristar II 3020 analyser using nitrogen as adsorbate at 77K. FT-IR spectra were recorded within the wavelength range of 4000-500 cm^{-1} using Perkin Elmer spectrum 100 FT-IR spectrometer while electronic spectra were reported using Cary100 UV-Visible spectrophotometer from Agilent Technology.

3. RESULT AND DISCUSSION

3.1 X-ray powder diffraction (XRD) of iron oxides nanoparticles

Powder XRD diffraction patterns are shown in **Fig. 1a-c**. The average particle sizes of the nanoparticles were calculated from the indexed peaks using Scherer formula [27]:

$$D = \frac{0.94\lambda}{\beta \mathrm{Cos}\ \theta}$$

Where β is the full width at half maximum (FWHM); D is the crystalline size (nm); θ is the angle of incidence; λ is the wavelength of diffraction (0.1546 nm). The magnetite diffraction pattern (Fig. 1a) was consistent with the standard structure of magnetite with reference no. (JCPDS Card No. 74-0748) [28] while maghemite diffraction patterns were indexed with the standard form of maghemite (JCPDS Card No. 25-1402)[29].

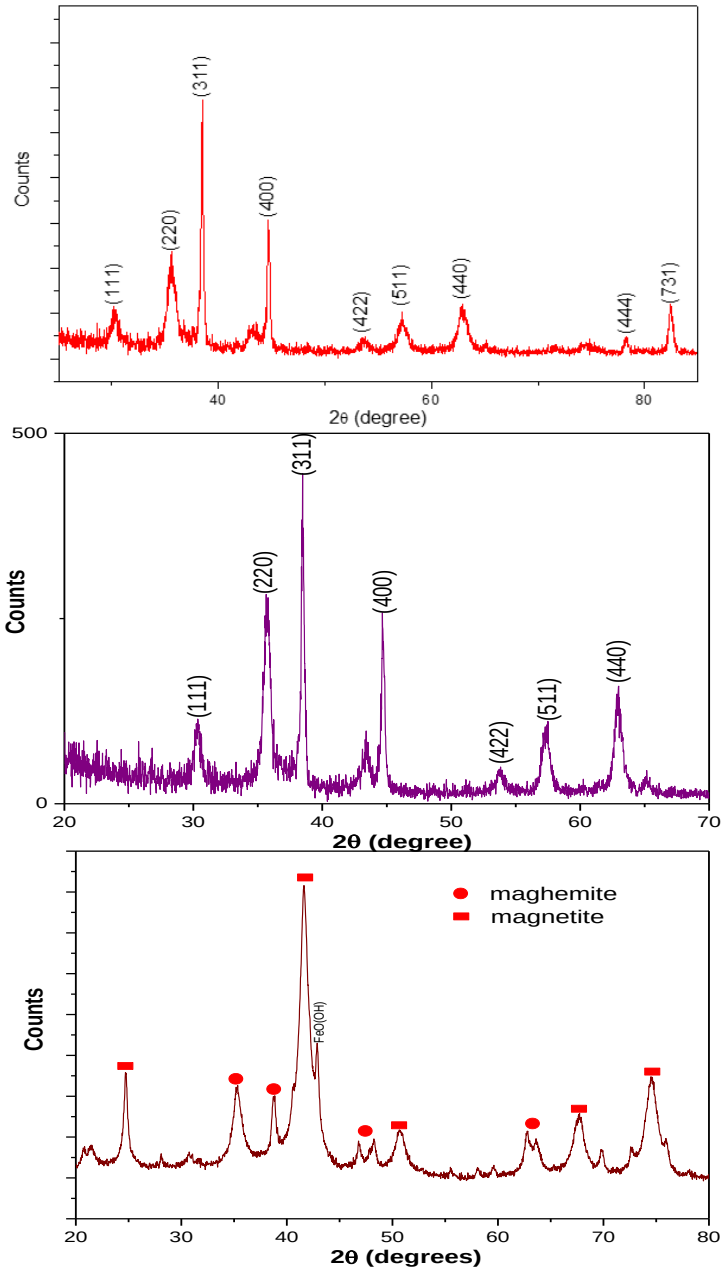

Figure I. (a) X-ray diffraction patterns for magnetite nanoparticles (b) X-ray diffraction patterns for maghemite nanoparticles (c) X-ray diffraction patterns of magnetite (NaOH).

The powder XRD diffraction patterns for magnetite nanoparticles showed no extra peak, suggesting a monophasic composition. The particle size of magnetite using the most intense peak (311) was 9.31 nm, while maghemite was 16.30 nm. A mixture of diffraction patterns corresponding to

different phases of iron nanoparticles was obtained when NaOH was used as precipitating base to prepare the iron oxide magnetic nanoparticles (Fig. 1c). The tail on the most intense peak is lepidocrocite (γ-FeO(OH)) [30, 31]. The crystallite size extrapolated from the most intense peak (311) was about 5 nm. For simplicity in presentation, magnetite synthesised using NaOH shall be hereafter referred to as magnetite (NaOH).

3.2 Cyclic and Square wave voltammetry of iron oxides nanoparticles

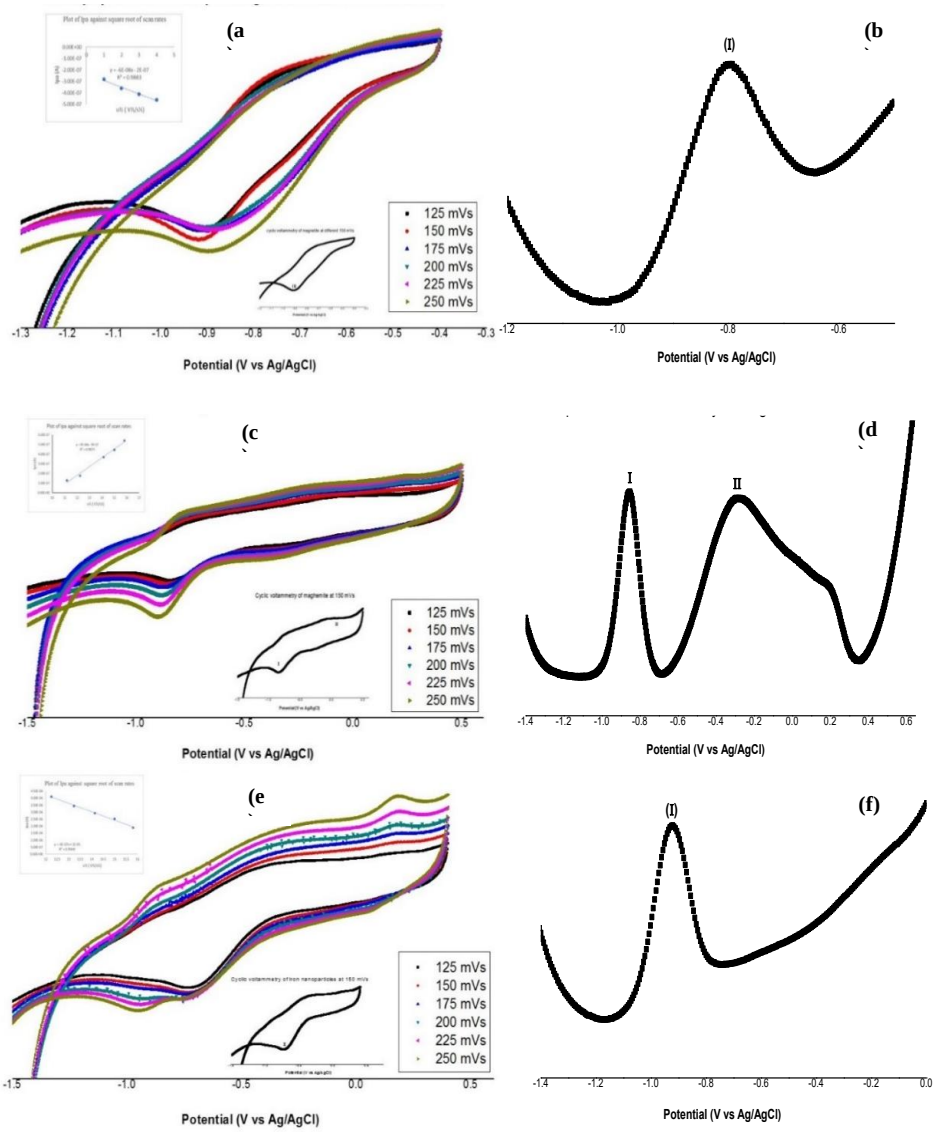

Figure 2. (a) Overlay cyclic voltammogram of magnetite at different scan rates; Insert: **Top**: plot of peak current vs. square root of scan rate; **bottom**: scan rate of magnetite at 150 mVs (b) Square wave voltammetry of magnetite at 100 mVs (c) Overlay cyclic voltammogram of maghemite at different scan rates; Insert: **Top**: plot of peak current vs. square root of scan rate; **bottom**: scan rate of maghemite at 150 mVs (d) Square wave voltammetry of maghemite at 100 mVs (e) Overlay cyclic voltammogram of magnetite (NaOH) at different scan rates; Insert: **Top**: plot of peak current vs. square root of scan rate; **bottom**: scan rate of magnetite (NaOH) at 150 mVs (f) Square wave voltammetry of magnetite (NaOH) at 100 mVs.

Cyclic voltammetry is a robust technique that can be used to determine secondary phase in nanoparticles [32]. The cyclic voltammograms of the nanoparticles (magnetite and maghemite) showed a redox couple for both magnetite and maghemite. However, maghemite besides had an irreversible anodic peak (**Fig. 2a and 2c**). The redox couple I in all nanoparticles have a broad peak to peak separation (ΔE values) that are considered quasi-reversible; redox couple II in maghemite is irreversible [33]. The presence of an irreversible anodic peak in maghemite is therefore indicative of the presence of a secondary phase in the nanoparticle. The signals were further confirmed from the square wave voltammetry of the nanoparticles (**Fig. 2b and 2d**). The redox couple is indicative of the electron transition between $Fe^{2+} \rightleftharpoons Fe^{3+}$.

Interestingly, cyclic voltammogram of magnetite (NaOH) (**Fig. 2e**), shows only one redox couple that indicate a monophase composition. This is further confirmed from the square wave voltammogram (**Fig. 2f**). Correlating cyclic voltametric report with the powder XRD diffraction patterns and lattice fringes of the nanoparticles, magnetite nanoparticles can be inferred to be the dominant phase present in magnetite (NaOH). Furthermore, the cyclic voltammogram of both forms of nanoparticles at 150 mVs (**Insert Fig. 2a and 2e**) matches. The low resolution of the diffraction peaks of magnetite (NaOH) as captured in the powder XRD (**Fig. 2c**) might have been due to low crystallinity of the synthesised nanoparticles. Plots of peak current against the square root of the scan rate for all nanoparticles (**Insert Fig. 2b, 2d, and 2f**) were linear which indicates that the redox couples were diffusion-controlled [33]. The cyclic and square wave voltametric study of the magnetite (NaOH) further confirmed that the dominant phase is magnetite.

3.3 HRTEM analysis of iron oxides nanoparticles

High resolution transmission electron microscopy (HRTEM) micrograph of magnetite nanoparticles (**Fig. 3a**) were spherical and slightly agglomerated; the magnetic property of the nanoparticles might have been responsible for the aggregation [28]. The particle size distribution range of 5.25 to 11.83 nm agreed well with the calculated particle size of 9.31 nm. Selected area electron diffraction (SAED) (**Insert, Fig. 3a**) showed consistent symmetrical dots which confirms that the as-prepared iron oxides nanoparticles are crystalline [34]. The observed lattice fringes value of 0.25 nm correlates with the lattice plane separation of diffraction peak indexed (311) [34]. Maghemite nanoparticles (**Fig. 3b**) were spherical and less agglomerated. The particle sizes were within the range of 9.63 to 16.45 nm, which correlates well with the particle size of 16.30 nm. The unsymmetric dots observed in the SAED for maghemite (**Insert, Fig. 3b**) indicates polycrystallinity of the as-prepared iron oxides nanoparticles similar to what was reported by Ariffin *et al*. for maghemite [35].

Comparatively, images for magnetite (NaOH) (**Fig. 3c**) contained mixtures of quasi-spherical and rod-like shaped iron oxides nanoparticles. The particles size range of 3.55 to 8.29 nm agreed with crystallite size of 5 nm obtained from the powder XRD. Lattice fringes of magnetite (NaOH) (**Insert Fig. 3c**) with an inter-fringe distance of 0.30 nm correlate with interplane distance (220) of the cubic spinel structure of magnetite [36]. Furthermore, the lattice fringe value of 0.27 nm approximate to the fringe distance of 0.25 nm for (311) plane [34]. This further confirms with the predominant magnetite

phase from the cyclic voltametric data. The blurred dotted lattice implies reduced crystallinity in contrast to magnetite nanoparticles (**Insert: Fig. 3c**).

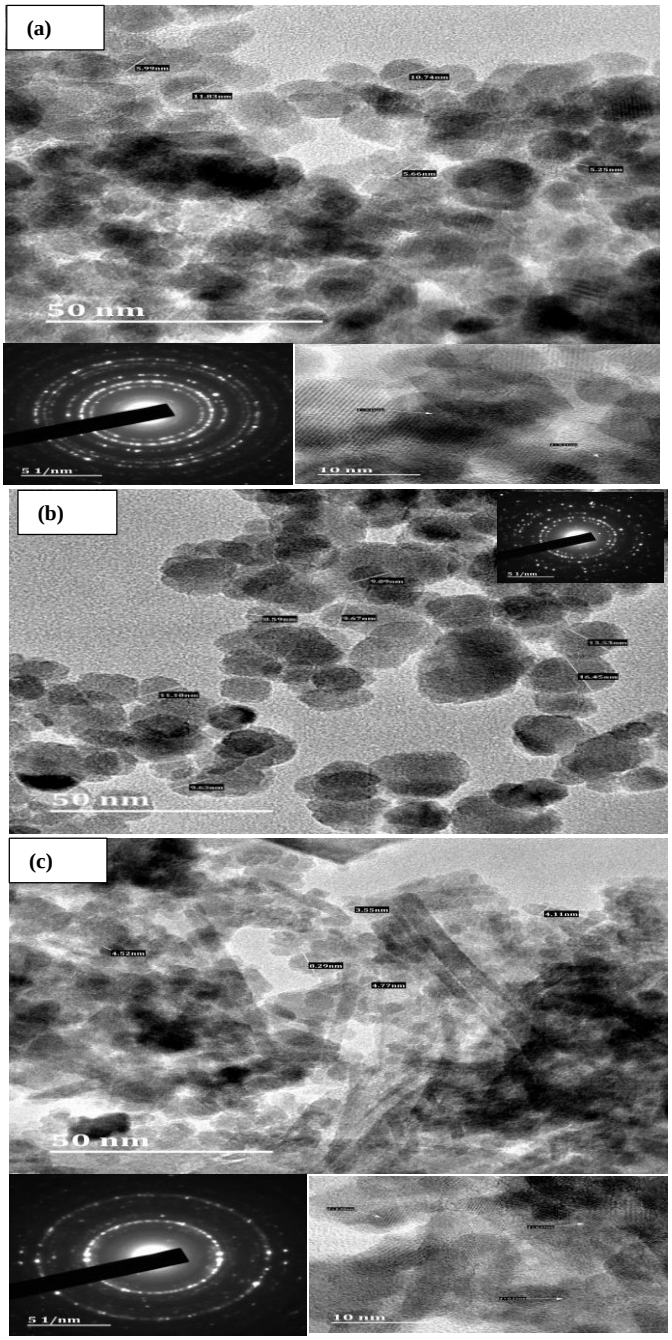

Figure 3. (a) HRTEM micrograph of magnetite; bottom left (SAED) bottom right (Lattice fringes) (b) HRTEM micrograph of maghemite, Insert: (SAED) (c) HRTEM micrograph of magnetite (NaOH); bottom left (SAED) bottom right (Lattice fringes).

3.4 SEM and EDX of iron oxides nanoparticles

SEM image of magnetite **(Supplementary Fig. 4a)** showed surface morphology was compact and unevenly distributed. Maghemite nanoparticles (**Supplementary Fig. 4c**) were flaky and dense while iron nanoparticles (**Supplementary Fig. 4e**) were coral-like and agglomerated.

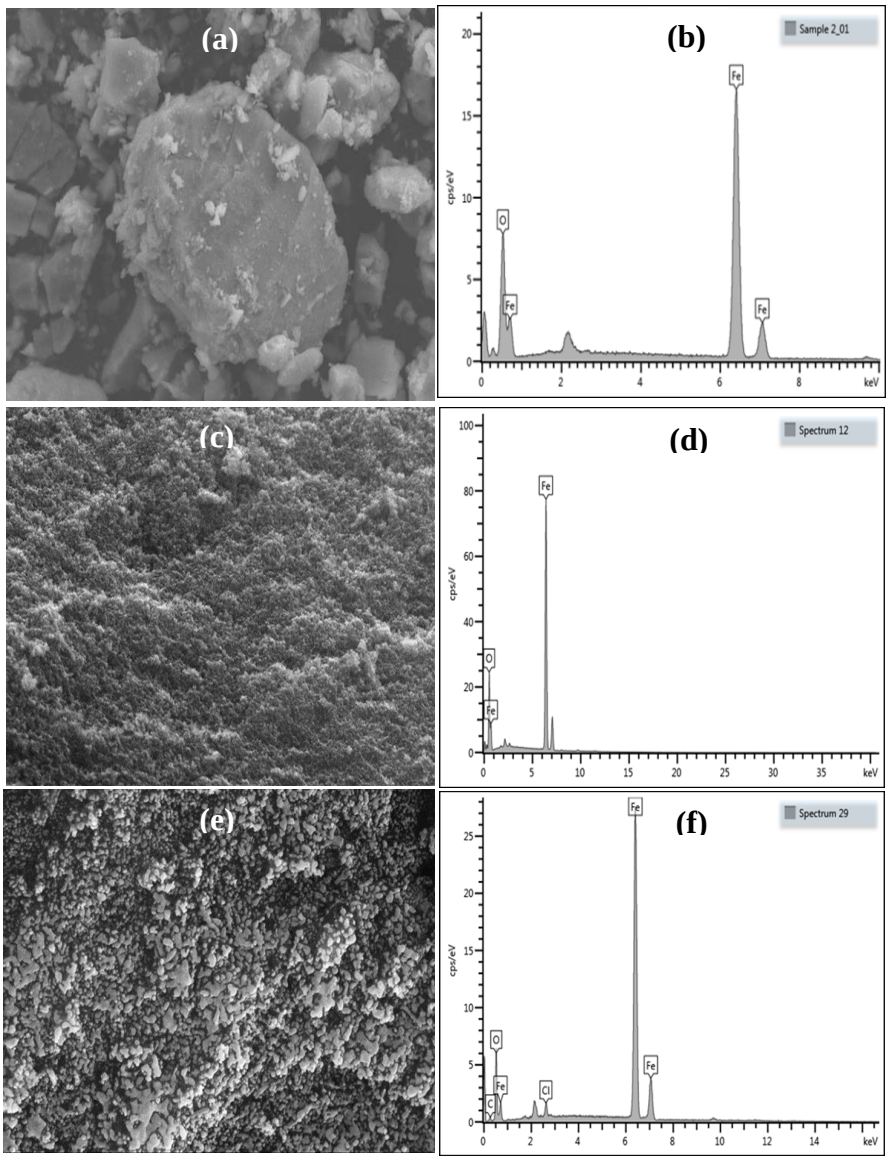

Figure 4: (a) SEM image of magnetite (b) EDX spectrum of magnetite (c) SEM image of maghemite (d) EDX spectrum of maghemite (e) SEM image of iron nanoparticles (f) EDX spectrum of iron nanoparticles

Weight percentages from the **EDX** spectrum of magnetite (**Fig. 4b**) were 76% Fe and 24% O while maghemite (**Fig. 4d**) was 63% Fe and 27% O respectively. The absence of foreign peaks communicates the atomic purity of both magnetite and maghemite. SEM and EDX images of magnetite (NaOH) (**Fig. 4e and 4f**) had atomic weight compositions of 83.54% Fe and 11.16% O; Cl is remnant from the precipitating base.

3.5 FTIR spectra studies of the iron oxides nanoparticles

The FTIR peak at 3219 cm^{-1} (**Fig. 5a**) is ascribed to O−H stretching from the hydrated magnetite iron oxide nanoparticles which was reduced to 3201 cm^{-1} in maghemite iron oxide nanoparticles. For magnetite (NaOH) , H−O−H bending vibration typical of water molecules with less intense peaks were observed at 1614 cm^{-1} and 1037 cm^{-1} as against 1618 cm^{-1} and 1046 cm^{-1} in magnetite and maghemite; these values agreed well with data reported by Lopez and co-authors [37].

Magnetite FTIR spectra typically show strong stretching vibrations near 570 cm^{-1} assigned to Fe−O bond [38]. The presence of strong stretching vibrations at 557 cm^{-1} (**Fig. 5a**) confirms magnetite. The maghemite (γ-Fe_2O_3) is characterized by absorption around 620 cm^{-1} [39]; absorption around 626 cm^{-1} is characteristic of maghemite. Characteristic absorption bands of Fe−O bond at 559 cm^{-1}, together with a shoulder at 704 cm^{-1} and the sharp peak at 795 cm^{-1} suggest a mixture of phases in magnetite (NaOH) [38].

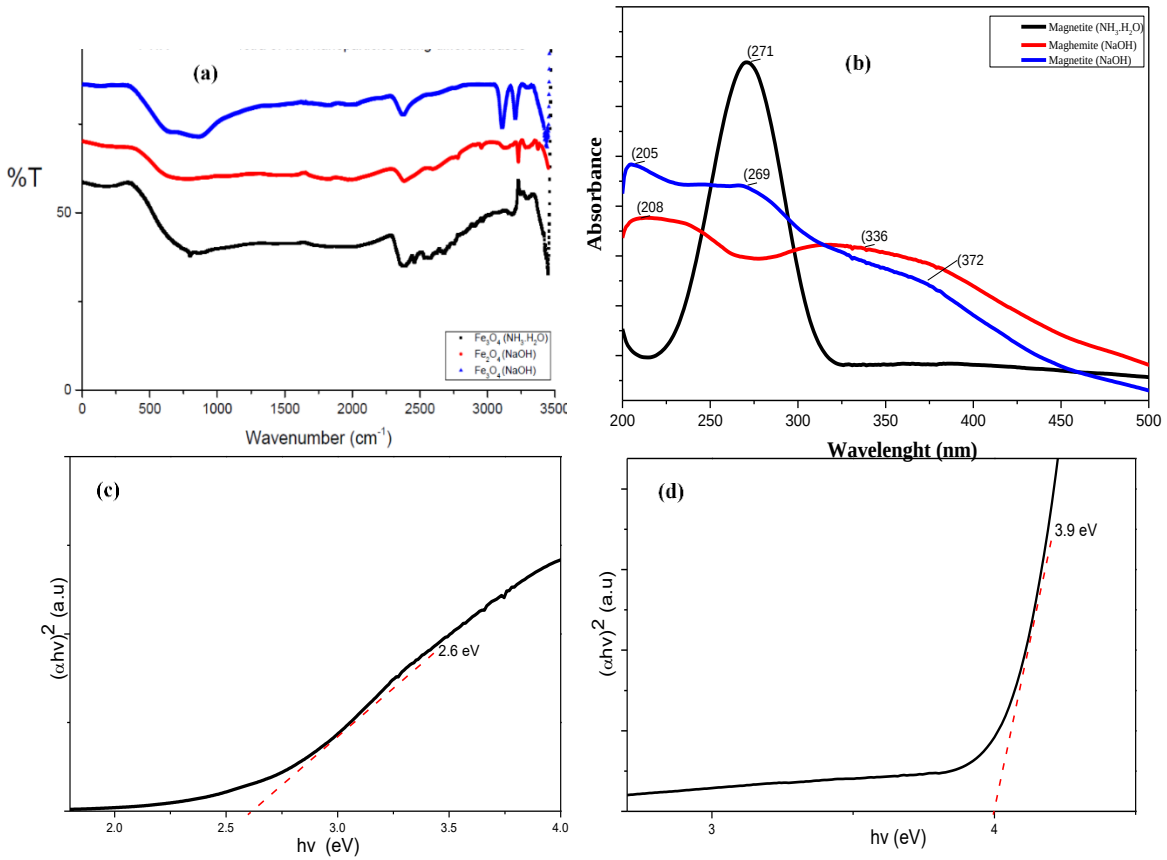

Figure 5. (a) Overlay FT – IR spectra of iron nanoparticles (b) Overlay electronic spectra of iron nanoparticles (c) band gap of maghemite (d) band gap of magnetite

3.6 Optical absorption and bandgap analysis of the iron oxides nanoparticles

Magnetite *iron oxides* nanoparticles showed a strong absorption band within 225 nm to 335 nm with peak height at 271 nm; maghemite nanoparticles showed distinct bands at 336 and 208 nm while

magnetite (NaOH) iron oxides displayed three absorption bands at 205, 269 and 372 nm respectively (**Fig. 5b**). The disappearance of magnetite characteristic electronic band from the overlay spectra when iron precursors were in molar ratio 1:1; confirms that absorption at 368 nm is for maghemite. Furthermore, the consistency and reproducibility of the bands in magnetite (NaOH) confirm that magnetite absorbs around 271 nm while maghemite absorbs at 372 nm. The Tauc's plot was used to extrapolate band gaps of the synthesized nanoparticles; the band gap value of maghemite was 2.6 eV as against 3.9 eV for magnetite when aqueous ammonia was used as precipitating base (**Fig. 5c & 5d**). However, the bandgap value of magnetite was reduced to 2.8 eV when NaOH was used as a precipitating base (**Fig. 6**).

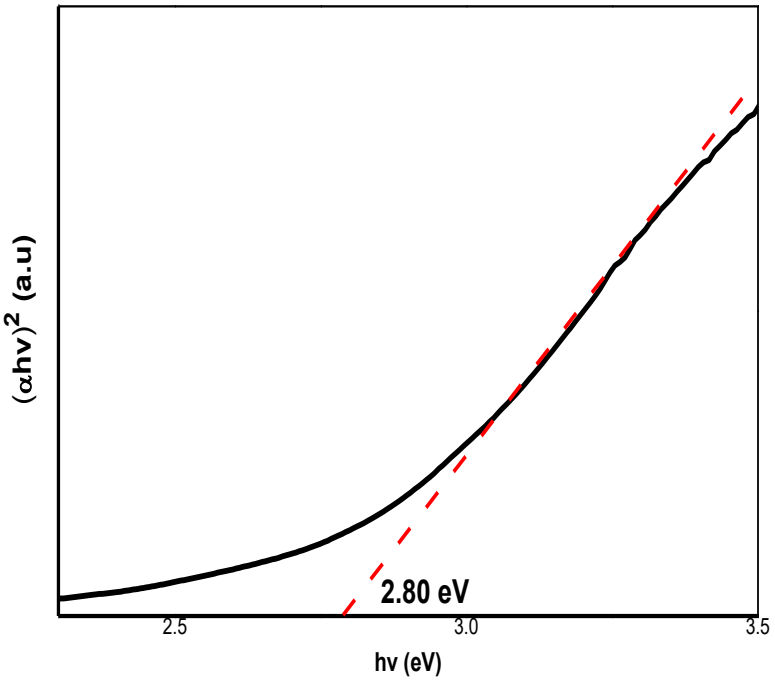

Figure 6. Tauc plot of $(ahv)^2$ against hv (eV) for magnetite nanoparticles synthesized using using NaOH as base

3.7 BET surface area of magnetite nanoparticles

The surface characteristic of magnetite was investigated by degassing 0.5 g of magnetite iron oxide nanoparticles at 200 °C for 8 h and comparing mass after cooling of the degassing process. Nitrogen adsorption-desorption plot (**Fig. 7a**) shows magnetite isotherm follows type V isotherm according to IUPAC classification [40]. Brunauer-Emmett-Teller's surface area (S_{BET}) of magnetite was 110.31 $m^2/g \pm 0.31$ m^2/g while the average pore volume was 0.36 cm^3/g. Bagbi *et al.* [27] had reported values of 73.28 m^2/g and 0.22 cm^3/g for S_{BET} and pore volume via a co-precipitation synthetic route. Pore distribution plot (**Fig. 7b**) were within the range of 2 – 50 nm; this implies that the particles were mesoporous with average pore size of 12.96 nm [41].

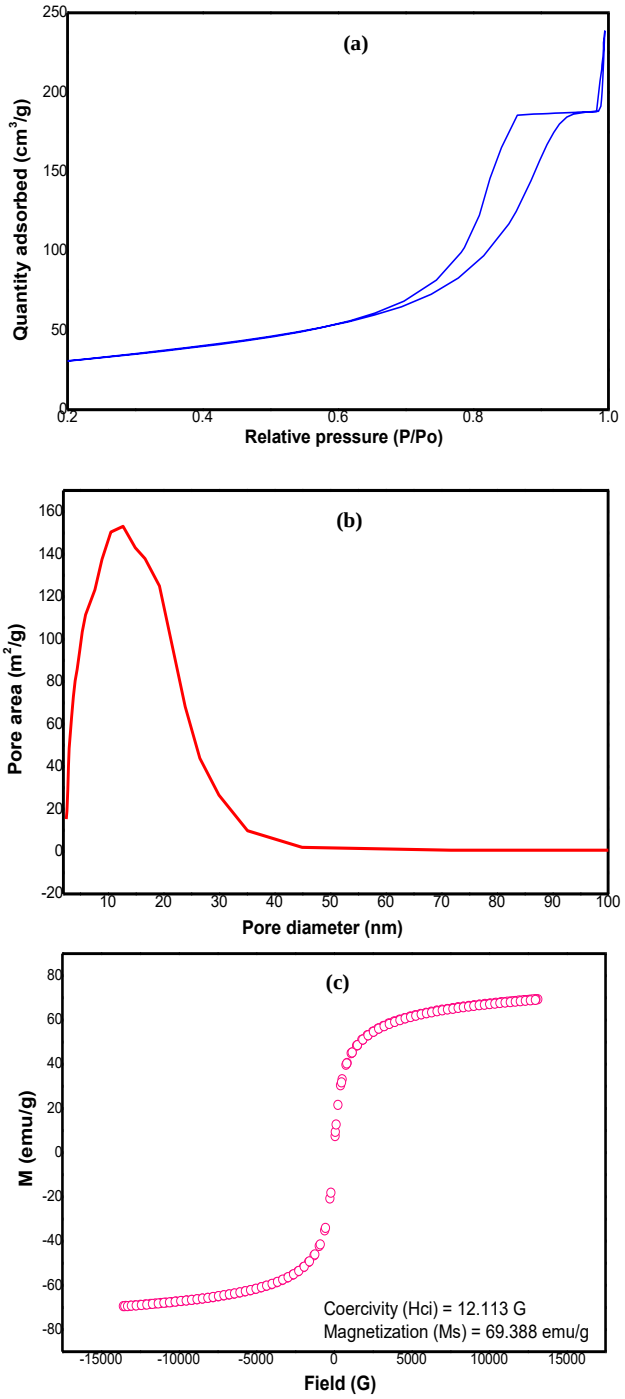

Figure 7. (a) Nitrogen adsorption-desorption isotherm for magnetite nanoparticles (b) size distribution plot of magnetite nanoparticles (c) magnetization curve for magnetite nanoparticles.

3.8 Magnetisation saturation of magnetite nanoparticles

Superparamagnetism is confirmed from the hysteresis loops of the magnetisation curve of magnetite (**Fig. 7c**). The reported value of 12.113G for coercivity and infinitesimal remnant magnetisation shows magnetite nanoparticles as superparamagnetic. Magnetisation saturation (Ms) value at 300K was 69.3 emu/g; this is close to the value of 68.8 emu/g reported by Wan *et al.* [34] for magnetite obtained via co-precipitation synthetic route.

4. CONCLUSION

Magnetite and maghemite nanoparticles were synthesized and their phases quantitatively identified using powder X-ray diffraction patterns cyclic and square wave voltammetry. Powder X-ray diffraction patterns of both magnetite and maghemite confirmed monophase composition, while cyclic voltammetry revealed a secondary phase in maghemite nanoparticles. The powder XRD of magnetite (NaOH) reflected a mixture of phases; however, cyclic voltammetry of the nanoparticle suggested a monophase composition. Furthermore, preliminary qualitative instrumentation such as FTIR, UV-Visible, and EDS was discussed as potential control tools to differentiate the phases of magnetite and maghemite iron oxides nanoparticles. Oxidative potentials of Fe(II) were more when sodium hydroxide was used as a precipitating base. This might be explained from its ionic composition; sodium hydroxide being electropositive and a strong base would have a stronger affinity for oxygen than aqueous ammonia, leading to the formation of oxy-hydroxides and oxidation of the reaction environment [38]. The study shows the importance of the application of cyclic voltammetry together with powder X-ray diffraction patterns to confirm the absolute phase of superparamagnetic iron oxide nanoparticles (SPION). Electrochemistry should be adopted together with powder X-ray diffractions to establish the dominant phase of reductive nanomaterials. Electrochemistry, FTIR and UV-Visible are desirable table tools applicable for the confirmation of phase integrity of iron oxide nanoparticles.

References

1. M. Colombo, S. Carregal-Romero, M.F. Casula, L. Gutiérrez, M.P. Morales, I.B. Böhm, J.T. Heverhagen, D. Prosperi and W.J. Parak, *Chem. Soc. Rev*., 41 (2012) 4306.
2. X. Qu, P.J. Alvarez and Q. Li, *Water Res.,* 47 (2013) 3931.
3. R.S. Yadav, I. Kuřitka, J. Vilcakova, J. Havlica, L. Kalina, P. Urbánek, M. Machovsky, D. Skoda, M. Masař and M. Holek, *Ultrason. Sonochem.,* 40 (2018) 773.
4. X. Sun, C. Zheng, F. Zhang, Y. Yang, G. Wu, A. Yu and N. Guan, *J. Phys. Chem. C,* 113 (2009) 16002.
5. S. Veintemillas-Verdaguer, M. Morales and C. Serna, *Appl. Organomet. Chem.,* 15 (2001) 365.
6. S. Rajput, L.P. Singh, C.U. Pittman Jr and D. Mohan, *J. Colloid Interface Sci.,* 492 (2017) 176.
7. M. Mahdavi, M.B. Ahmad, M.J. Haron, F. Namvar, B. Nadi, M.Z.A. Rahman and J. Amin, *Molecules,* 18 (2013) 7533.
8. I. Bibi, S. Kamal, A. Ahmed, M. Iqbal, S. Nouren, K. Jilani, N. Nazar, M. Amir, A. Abbas and S. Ata, *Int. J. Biol. Macromol.,* 103 (2017) 783.
9. S. Sun and H. Zeng, *J. Am. Chem. Soc.,* 124 (2002) 8204.
10. S.R. Kumar, M. Paulpandi, M. ManivelRaja, D. Mangalaraj, C. Viswanathan, S. Kannan and N. Ponpandian, *RSC Adv.,* 4 (2014) 13409.
11. X.L. Liu, H.M. Fan, J.B. Yi, Y. Yang, E.S.G. Choo, J.M. Xue, D. Di Fan and J. Ding, *J. Mater. Chem. A,* 22 (2012) 8235.
12. A.A. Hernández-Hernández, G.A. Álvarez-Romero, A. Castañeda-Ovando, Y. Mendoza-Tolentino, E. Contreras-López, C.A. Galán-Vidal and M.E. Páez-Hernández, *Mater. Chem. Phys.,* 205 (2018) 113.
13. R. Lakshmanan, C. Okoli, M. Boutonnet, S. Järås and G.K. Rajarao, *J. Environ. Chem. Eng.,* 2 (2014) 185.

14. F. Vereda, J. de Vicente and R. Hidalgo-Alvarez, *J. Colloid Interface Sci.,* 392 (2013) 50.
15. W. Schärtl, *Nanoscale,* 2 (2010) 829.
16. E.C. Nnadozie and P.A. Ajibade, *Molecules,* 25 (2020) 4110.
17. S.A. Wahajuddin, *Int. J. Nanomed.,* 7 (2012) 3445.
18. J. Azadmanjiri, G.P. Simon, K. Suzuki, C. Selomulya and J.D. Cashion, *J. Mater. Chem*., 22 (2012) 617.
19. Y. Chen, Z. Lai, X. Zhang, Z. Fan, Q. He, C. Tan and H. Zhang, *Nat. Rev. Chem.,* 4 (2020) 243.
20. D. Maiti, U. Manju, S. Velaga and P.S. Devi, *Cryst. Growth Des.,* 13 (2013) 3637.
21. E.A. Campos, D.V.B.S. Pinto, J.I.S. de Oliveira, Ed.C. Mattos and R.C.L. Dutra, *J. Aerosp. Technol. Manag.,* 7 (2015) 267.
22. R. Hufschmid, H. Arami, R.M. Ferguson, M. Gonzales, E. Teeman, L.N. Brush, N.D. Browning and K.M. Krishnan, *Nanoscale,* 7 (2015) 11142.
23. K. Matusiak, A. Drozdz, Z. Setkowicz, A. Kubala-Kukus, I. Stabrawa, M. Ciarach, K. Janeczko, D. Horak, M. Babic and J. Chwiej, *Metallomics*, 12 (2020) 1811.
24. M.A. Dheyab, A.A. Aziz, M.S. Jameel, O.A. Noqta, P.M. Khaniabadi and B. Mehrdel, *Sci. Rep*., 10 (2020) 10793.
25. S.K. Behera, S. Sahni, G. Tiwari, A. Rai, B. Mahanty, A. Vinati, E.R. Rene and A. Pugazhendhi, *Appl. Sci.,* 10 (2020) 3181.
26. V. Wanjeri, C. Sheppard, A. Prinsloo, J. Ngila and P. Ndungu, *J. Environ. Chem. Eng.,* 6 (2018) 1333.
27. Y. Bagbi, A. Sarswat, D. Mohan, A. Pandey and P.R. Solanki, *J. Environ. Chem. Eng.,* 4 (2016) 4237.
28. M.C. Mascolo, Y. Pei and T.A. Ring, *Materials,* 6 (2013) 5549.
29. S.-J. Lee, J.-R. Jeong, S.-C. Shin, J.-C. Kim and J.-D. Kim, *J. Magn. Magn. Mater*., 282 (2004) 147.
30. L. Tijing, M. Ruelo, C.-H. Park, A. Amarjargal, H. Kim, H. Pant, D.-H. Lee and C. Kim, *Chem. Pap.,* 67 (2013) 1304.
31. M. Aliahmad and N.N. Moghaddam, *Mater. Sci.-Pol.*, 31 (2013) 264.
32. F.J. Santos, L.C. Varanda, L.C. Ferracin and M. Jafelicci, *J. Phys. Chem. C,* 112 (2008) 5301.
33. S. Chohan, I.N. Booysen, A. Mambanda and M.P. Akerman, *Inorg. Chim. Acta,* 447 (2016) 183.
34. J. Wan, G. Tang, Y. Qian, *Appl. Phys. A,* 86 (2007) 261.
35. M.F.K. Ariffin, A. Idris and N.H.A. Ngadiman, *Brazilian J. Chem. Eng*., 36 (2019) 171.
36. M.I. Khalil, *Arab. J. Chem.* 8 (2015) 279.
37. J.A. Lopez, F. González, F.A. Bonilla, G. Zambrano and M.E. Gómez, *Rev. LatinAm. Metal. Mater.,* 30 (2010) 60.
38. G.V. Jacintho, A.G. Brolo, P. Corio, P.A. Suarez and J.C. Rubim, *J. Phys. Chem. C,* 113 (2009) 7684.
39. S. Nasrazadani and H. Namduri, *Spectrochim. Acta B: At. Spectrosc*., 61 (2006) 565-571.
40. K.S. Sing, *Pure Appl. Chem.,* 57 (1985) 603.
41. M. Thommes, *Chem. Ing. Tech.,* 82 (2010) 1059.

© 2022 The Authors. Published by ESG (www.electrochemsci.org). This article is an open access article distributed under the terms and conditions of the Creative Commons Attribution license (http://creativecommons.org/licenses/by/4.0/).